ADVANCED ENERGY MATERIALS
www.advenergymat.de

Size-Controlled Synthesis of IrO_2 Nanoparticles at High Temperatures for the Oxygen Evolution Reaction

Marko Malinovic, Paul Paciok, Ezra Shanli Koh, Moritz Geuß, Jisik Choi, Philipp Pfeifer, Jan Philipp Hofmann, Daniel Göhl, Marc Heggen, Serhiy Cherevko, and Marc Ledendecker**

Iridium oxide is the state-of-the-art catalyst for electrochemical water oxidation in an acidic medium. Despite being one of the rarest elements in the Earth's crust, there is a pressing need to maximize the utilization and longevity of active iridium centers. While conventional low-temperature synthesis can yield nanostructures with high mass-specific activity, they are often insufficiently stable during water oxidation. Structurally ordered iridium oxide is one of the most stable electrocatalysts utilized in polymer electrolyte membrane water electrolysis that benefits from the chemically ordered structure. However, its preparation requires thermal treatment at high temperatures, which improves its durability but can also result in reduced surface area and altered particle morphology. In this study, the challenge of controlling nanoparticle size during the preparation of structurally ordered iridium oxide is successfully addressed, which typically requires high-temperature thermal treatment. By utilizing a silica nanoreactor as a hard template, a precise control is achieved over the nanoparticle size during high-temperature thermal treatment. This approach maintains high durability while avoiding the common problem of reduced surface area and altered particle morphology. Specifically, this study is able to synthesize iridium oxide nanoparticles at temperatures up to 800 °C, while keeping their dimensions below 10 nm.

1. Introduction

Polymer electrolyte membrane water electrolysis (PEM-WE) is considered to be a cornerstone for the sustainable generation of hydrogen.[1,2] The efficiency of the process, however, is still insufficient and largely influenced by the sluggish kinetics of the oxygen evolution reaction (OER) at the anode. To overcome this, researchers have turned to noble metal catalysts such as iridium and ruthenium oxide, which are currently considered state-of-the-art materials. While ruthenium oxide shows higher catalytic activity under the harsh conditions of low pH and high anodic operating potential, iridium oxide is more dissolution resistant, offering a better compromise between electrochemical activity and stability.[3,4] At the same time, scaling-up PEM-WE to Gigawatt level using scarce noble metal catalysts demands maximized catalyst utilization and extension of operation times.[5,6] For iridium-based materials,

M. Malinovic, J. Choi, D. Göhl
Technical University of Darmstadt
Department of Chemistry
Ernst-Berl-Institut für Technische und Makromolekulare Chemie
64287 Darmstadt, Germany
E-mail: marko.malinovic@tum.de
P. Paciok, M. Heggen
Ernst Ruska-Centre (ER-C-1)
Forschungszentrum Jülich GmbH
Leo Brandt Straße 1, 52428 Jülich, Germany

M. Malinovic, E. S. Koh, J. Choi, P. Pfeifer, M. Ledendecker
Technical University Munich
Campus Straubing
Sustainable Energy Materials
Schulgasse 22, 94315 Straubing, Germany
E-mail: marc.ledendecker@tum.de
M. Geuß, S. Cherevko, M. Ledendecker
Helmholtz Institute Erlangen-Nürnberg for Renewable Energy
Forschungszentrum Jülich GmbH
Cauerstraße 1, 91058 Erlangen, Germany
J. P. Hofmann
Surface Science Laboratory
Department of Materials and Earth Sciences
Technical University of Darmstadt
Otto-Berndt-Straße 3, 64287 Darmstadt, Germany

The ORCID identification number(s) for the author(s) of this article can be found under https://doi.org/10.1002/aenm.202301450

DOI: 10.1002/aenm.202301450

different catalysts have been studied to address this challenge ranging from amorphous[7] and crystalline iridium oxide[8] to perovskites,[9] pyrochlores,[10] or hollandites.[11] Despite promising OER activity of amorphous iridium oxide and iridium-based perovskites, their durability remains a major challenge and a long-term operation is questionable.[12] Structurally ordered iridium oxide in the rutile structure ($IrO_{2\text{-rutile}}$) belongs to the most dissolution-resistant catalysts under OER conditions with orders of magnitude higher stability compared to its amorphous and perovskite counterparts.[13] The compact rutile structure with strong Ir–O bonds is not easily destabilized.[14–16] Raising the calcination temperature can enhance the stability of the catalyst by eliminating structural defects and promoting greater ordering and long-range arrangement of atoms within the catalyst.[4] The disadvantage of crystalline $IrO_{2\text{-rutile}}$ lies in the low catalytically active surface area availability since the high crystallinity prevents the utilization of underlying "sub-surface" iridium centers. This leads to a high necessary overvoltage and therefore low efficiency. Highly crystalline materials with high surface-to-volume ratios are desired to combine high activity with high durability. However, high calcination temperatures inevitably induce a decrease in the surface area.[8,17,18] Novel synthesis routes are required to obtain highly crystalline and ordered iridium oxide while keeping the nanoparticle dimensions. Classical synthesis methods encompass hydrolysis in alkaline media,[19] sol–gel formation,[20] or precipitation in a microemulsion.[21] However, the reaction conditions are usually mild and temperatures below 100 °C typically result in oxide nanoparticles with low crystallinity and a high share of defects. Much attention was drawn to hydrous iridium oxide, obtained during continuous potential cycling of metallic iridium. Despite remarkable OER activity, the stability is inferior compared to thermally prepared iridium oxide.[12] The Adams' fusion method has been effective in synthesizing crystalline iridium oxide, but its application has been limited by the uncontrolled growth of particles and morphological changes that occur at temperatures ≥500 °C.[8] As the particle sizes change with calcination time and temperature, a fair comparison of structure performance indicators from nanoparticles synthesized at different temperatures cannot be obtained.

Here, we report the preparation of iridium oxide nanoparticles with preserved size and morphology after thermal treatment at temperatures up to 800 °C. The synthesis is based on the hydrolysis of iridium precursor in a water-in-oil microemulsion followed by a sol–gel encapsulation with silica. Changes in surface properties at different temperatures were tracked by X-ray photoelectron spectroscopy (XPS), the crystal structure was investigated by X-ray diffraction analysis (XRD), size and morphology were characterized by high-angle annular dark-field scanning transmission electron microscopy (HAADF-STEM) and high resolution scanning transmission electron microscopy (HR-STEM). A detailed understanding of the nanoparticle dynamics during heating was obtained by in situ scanning transmission electron microscopy (in situ STEM) with locally resolved nanoparticles, high spatial resolution, and chemical specificity. The OER activities of synthesized iridium oxide nanoparticles were measured in half-cell measurements at forced convection. The stability was probed by operando scanning flow cell (SFC) measurements that were coupled to an inductively coupled plasma mass spectrometer (ICP-MS). This is the first approach to generate iridium oxide nanoparticles with similar size and morphology at high temperatures and allows for the determination of activity and durability.

2. Results and Discussion

In a typical synthesis, we synthesized iridium oxide nanoparticles via a water-in-oil reverse microemulsion at ambient conditions. During the four-step process, as shown in **Figure 1**a, the iridium precursor was first hydrolyzed to hydrated iridium oxyhydroxide ($IrO_{1.45}(OH)_{1.10}{}^{*}1.5H_2O$) at room temperature and pH 10–11. The dispersed iridium-based aqueous solution was mixed with an *n*-heptane-surfactant (Brij 30) mixture followed by hydrolyzation of tetraethyl orthosilicate (TEOS) to form the encapsulating silica shell. Prior to thermal treatment, synthesized iridium oxyhydroxide nanoparticles were washed with acetone to remove surfactant residues and dried in air.

To start with the same material and to ensure similar particles sizes, the total sample amount was divided into three equal fractions and thermally treated in synthetic air at 400, 600, and 800 °C with a 2 °C min^{-1} temperature ramp followed by a 3 h hold at the respective temperature. The protecting silica shell is removed in a hydrofluoric acid-ethanol solution to obtain unsupported, surfactant-free iridium oxide nanoparticles.

To monitor the temperature-dependent mass loss, thermogravimetric analysis (TGA) analysis of the as-synthesized sample was performed up to 1100 °C (Figure S1, Supporting Information). During the first weight loss in the region of 100 °C, chemisorbed water is released. The weight loss between 200 and 800 °C is a joined effect of silanol condensation, surfactant decomposition, and oxidation of iridium oxyhydroxide.[22] Above 900 °C, a weight loss of 3.23% may indicate partial decomposition of iridium oxide to bare iridium metal.[23,24]

The silica encapsulated IrO_x ($IrO_x@SiO_2$) materials were characterized by ex situ HAADF-STEM (Figure 1b–d). and HR-STEM (Figure 1e–g) measurements to determine particle size distribution and morphology. At 400 °C (Figure 1b), multiple iridium oxide nanoparticles with a Sauter mean dimeter of 3.5 ± 0.8 nm (Figure S2a, Supporting Information) are clustered within a single silica sphere. While the HR-STEM image obtained (Figure 1e) suggested the presence of some degree of order in the particles, the level of crystallinity could not be conclusively determined based solely on the micrographs. With the increase in temperature to 600 (Figure 1c) and 800 °C (Figure 1d), the nanoparticles within the silica spheres unite and form one central aggregate. For both, the particle sizes are similar with a Sauter mean diameter of 7.7 ± 1.0 nm for IrO_2 calcined at 600 °C (Figure S2b, Supporting Information) and 7.4 ± 1.1 nm for IrO_2 calcined at 800 °C (Figure S2c, Supporting Information). Raising the temperature resulted in a noticeable improvement in the crystallinity of the iridium oxide nanoparticles, as revealed by the HR-STEM images (Figure 1f,g). By analyzing the atomic arrangement, the interplanar distance could be accurately determined, which in the case of IrO_2 calcined at 600 °C (Figure 1f) was found to correspond to the (101) lattice plane orientation. More comprehensive information on the size and morphology of the synthesized nanoparticles, subjected to different annealing temperatures, can be found in Figures S3–S5 (Supporting Information).

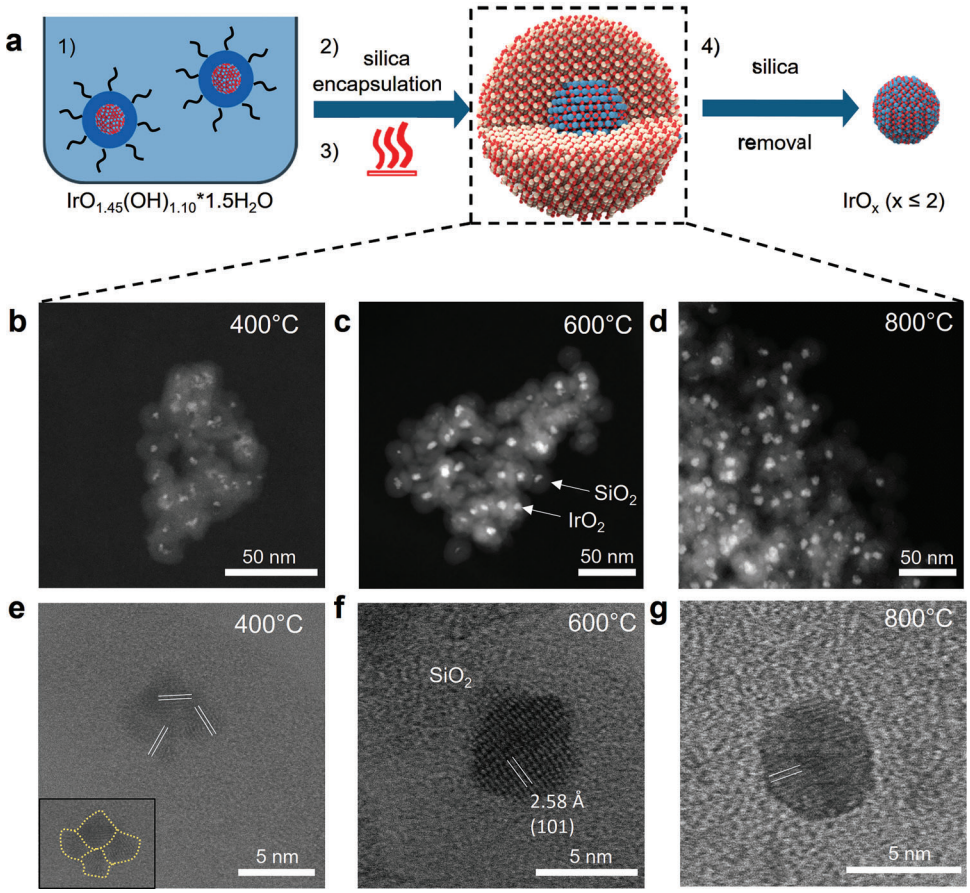

Figure 1. a) Schematic synthesis route of IrO_x nanoparticles. Ex situ HAADF-STEM images of IrO_x nanoparticles encapsulated in the silica shell thermally treated at b) 400, c) 600, and d) 800 °C, white arrows indicating IrO_2 and SiO_2 phases. HR-STEM images of IrO_x nanoparticles encapsulated in the silica shell thermally treated at e) 400 °C and the associated grain boundaries between domains (inset), f) at 600 °C, and g) at 800 °C.

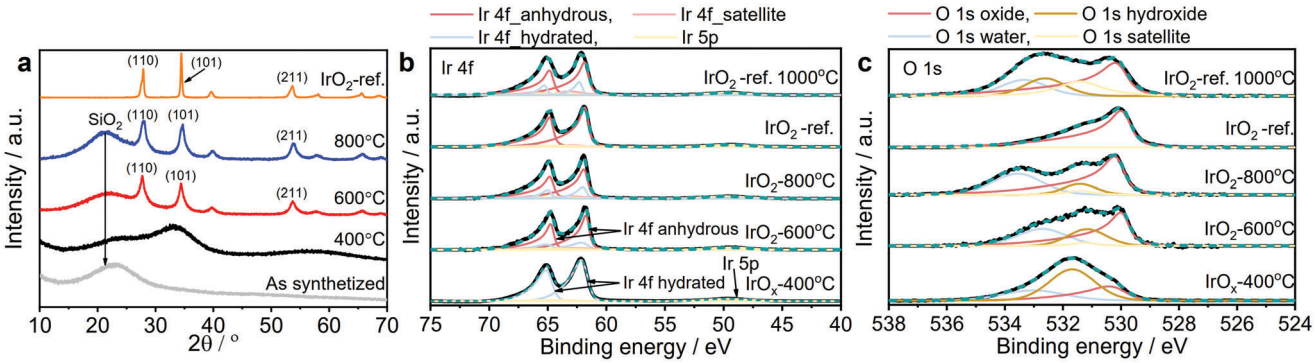

Figure 2. a) XRD patterns (Cu K_α radiation) of IrO_x@SiO_2 samples at room temperature, 400, 600, and 800 °C and IrO_2-ref. Miller indices indicated for the three most intense reflexes of the sample. XPS analysis b) Ir 4f core-level spectra and (c) O 1s core-level spectra of silica-free IrO_x nanoparticles prepared at 400 (IrO_x-400 °C), 600 (IrO_2-600 °C), and 800 °C (IrO_2-800 °C)and IrO_2-ref. IrO_2-ref. was additionally thermally treated at 1000 °C (IrO_2-ref. 1000 °C) with a 2 °C min^{-1} temperature ramp for 3 h in synthetic air atmosphere.

We performed a more detailed characterization of specifically selected specimens calcined at 400, 600, and 800 °C to further understand the impact of temperature on the material's structure. XRD analysis of the as-prepared sample (**Figure 2**a) prior to thermal treatment revealed the amorphous character of hydrous iridium oxyhydroxide as only the broad silica peak at ≈21.8° could be observed. The XRD diffraction pattern of IrO_x calcined at 400 °C (Figure 2a) consists of broad peaks that corroborate the formation of small and non-structurally ordered nanoparticles observed by ex situ HAADF-STEM analysis. The typical tetragonal rutile diffraction peaks of IrO_2 develop at 600 °C. The observed reflexes in Figure 2a are consistent with the HR-STEM images shown

in Figure 1f, which clearly revealed the (101) lattice spacing of $IrO_{2\text{-rutile}}$.

An increase in temperature to 800 °C did not affect the peak width suggesting that no significant alteration in crystallite size took place.[3,8] The substantially narrower reflexes of the reference IrO_2 catalyst from Sigma Aldrich (IrO_2-ref.) indicate larger crystallite size compared to synthesized samples. For an estimation of crystallite size, Scherrer's equation was applied to the three main diffractions (110, 101, and 211) of both IrO_2 calcined at 600 and 800 °C. We observe only slight differences in the mean crystallite size between samples ranging from 7.2 to 7.3 nm. In literature, higher calcination temperatures not only influence the overall size of the nanoparticles but also their morphology. At temperatures ≥500 °C, Abbott et al. observed the formation of thermodynamically favored rod-shaped particles predominantly growing in the (001) and (112) direction.[8] For the here presented samples, a preferred growth was not observed, arguably due to the confining silica matrix suppressing the growth of shape controlled nanoparticles. Complementary to ex situ HAADF-STEM and HR-STEM, XRD results suggest excellent control over the nanoparticle's size and morphology over a large temperature range.

To evaluate the chemical state of the near-surface and track the transformation of the surface species influenced by the respective thermal treatment, we performed ex situ XPS measurements of selected specimen (IrO_x-400 °C, IrO_2-600 °C and IrO_2-800 °C) after removal of the silica shell. The obtained results were compared to the IrO_2-ref. and IrO_2-ref. 1000 °C. Detailed Ir 4f and O 1s spectra were curve-fitted according to the fitting parameters from the work of Freakley et al.[25] Figure 2b shows the Ir 4f region of the analyzed samples featuring two asymmetric components, which in the case of IrO_2-600°C and IrO_2-800 °C are attributed to Ir $4f_{5/2}$ and Ir $4f_{7/2}$ at 61.9 and 64.9 eV, respectively. These values are in good agreement with the reference IrO_2 and were assigned to rutile IrO_2.[26] The slightly broader shape of Ir 4f peaks and shift to higher binding energies of 62.1 eV (65.1 eV) observed for the IrO_x-400 °C sample compared to the IrO_2-600 °C and IrO_2-800 °C might indicate the presence of mixed Ir (III) and Ir (IV) oxidation states.[8,25] The broad peak located at 531.7 eV in the O 1s spectrum (Figure 2c) suggests that the surface of IrO_x-400 °C is predominately hydroxyl-terminated. The increase in temperature induces the formation of the additional peak in the lower binding energy region. The peak in the case of the IrO_2-800 °C sample is located at ≈530.1 eV corresponding to the literature value (≈530.0 eV) for lattice oxygen, thus suggesting that the hydroxyl species at temperatures ≥400 °C are gradually replaced by lattice oxygen.[12,27,28] O1s spectra of IrO_2-600, IrO_2-800 °C, and the reference catalyst calcined at 1000 °C exhibit an additional peak at higher binding energies (≈533 eV). The origin of this peak is attributed to adsorbed water, which likely originated from the sample preparation procedure prior to XPS in aqueous media.

In order to better understand the structure-temperature relation of iridium oxide nanoparticles and the role of protecting silica matrix, we additionally synthesized iridium oxyhydroxide nanoparticles using the reverse microemulsion method, as previously described, but without addition of silica precursor (c.f. 4.1.2). We refer to this sample as bare iridium oxide. To obtain direct comparison of silica-encapsulated and bare iridium oxide nanoparticles and their structure evolution during the thermal treatment, we performed in situ STEM heating experiment under oxygen atmosphere with 3 °C s^{-1} temperature ramp and 30 min annealing at 200, 400, 600, and 800 °C thus obtaining unique real-time insight into the temperature dependent structural evolution of $IrO_x@SiO_2$ and bare iridium oxide nanoparticles. During the recording, we extracted STEM snapshots (**Figure 3**a–d) describing the behavior of the same $IrO_x@SiO_2$ clusters over the whole temperature range up to 800 °C. At lower temperatures, as shown by the example at 200 °C (Figure 3a; Movie S1, Supporting Information), individual silica shells comprise multiple ultra-small iridium oxide nanoparticles, similar to what we observed by ex situ HAADF-STEM for IrO_x calcined at 400 °C (Figure 1b). During in situ STEM with a temperature increase from 200 to 400 °C (Figure 3b; Movie S2, Supporting Information), the nanoparticles start to unite and grow together into a single aggregate at 600 °C (Figure 3c; Movie S3, Supporting Information). Faster aggregation of the nanoparticles compared to ex situ HAADF-STEM can be explained by different heating parameters, i.e., faster temperature ramp. Notably, the size of single aggregates within the silica spheres remains almost unchanged when the temperature is further increased to 800 °C (Figure 3d; Movie S4, Supporting Information).

Contrary to $IrO_x@SiO_2$, we observed uncontrolled growth of unprotected bare iridium oxide nanoparticles upon heating (Figure 3e–h). Aggregation of individual iridium oxide nanoparticles at temperatures ≥200 °C consequently resulted in the formation of large irregularly-shaped agglomerates reaching the ≈30 nm in size. This experiment confirms the central and pivoting role of the silica protecting shell on the final catalyst size and morphology during the thermal treatment.

After obtaining first insights into the catalyst's structure and surface species, we studied the impact of calcination temperature on the electrochemical OER activity of the synthesized catalysts after removing the silica shell. For the comparison in OER activity, following the conditioning steps (c.f. Table S1, Supporting Information), the very first polarization curve was used to avoid accumulation of oxygen bubbles at high current density blocking active sites.[29] The OER activities of all samples were determined at 900 rpm in 0.1 M $HClO_4$ and compared to IrO_2-ref. The application-relevant mass normalized current density throughout the applied potential range is shown in **Figure 4**b. IrO_x-400 °C outperforms all catalysts and is 40 times more active compared to IrO_2-ref. at E = 1.50 V_{RHE}. The higher OER activity of amorphous IrO_x-400 °C compared to crystalline IrO_2-600, IrO_2-800 °C and IrO_2-ref. samples is in agreement with literature for powders and thin films.[12,27,30,31] The significantly higher OER activity of IrO_x-400 °C in comparison to its crystalline counterparts cannot be solely explained by greater surface area, but the key factor is arguably the amorphous nature of IrO_x-400 °C. Operando X-ray absorption studies reported previously, suggest that the mixed charge state of Ir in amorphous IrO_x and the resulting increased surface coverage with hydroxide species are primarily responsible for the enhanced OER activity of amorphous IrO_x.[8,30,32] Willinger et al.[7] suggested that amorphous IrO_x has more activated oxygen species responsible for high OER activity. In line with XRD and XPS results, the cyclicvoltammogram (CV) resembles the shape of hydrous iridium oxide or amorphous iridium oxide. The characteristic A1/C1-A3/C3 redox couples between 0.6 V and

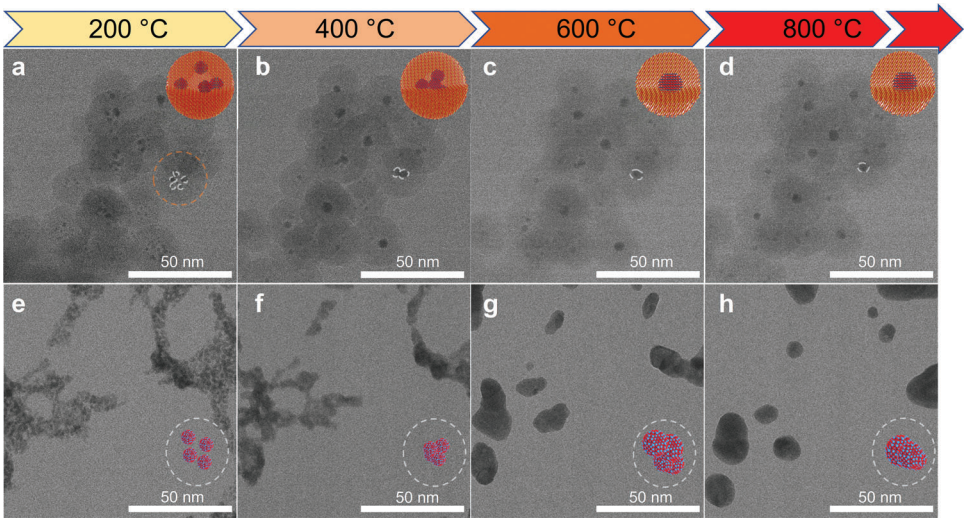

Figure 3. Structural evolution comparison between silica encapsulated (IrO_x@SiO_2) and bare iridium oxide nanoparticles during in situ heating STEM experiment. a–d) Selected STEM snapshots of IrO_x@SiO_2 and e–h) bare iridium oxide nanoparticles taken during in situ consecutive heat treatment in oxygen atmosphere at 200, 400, 600, and 800 °C. The illustrative inset sequence highlights the temperature-induced structural evolution of the iridium oxide nanoparticles with or without encapsulation in protecting silica matrix.

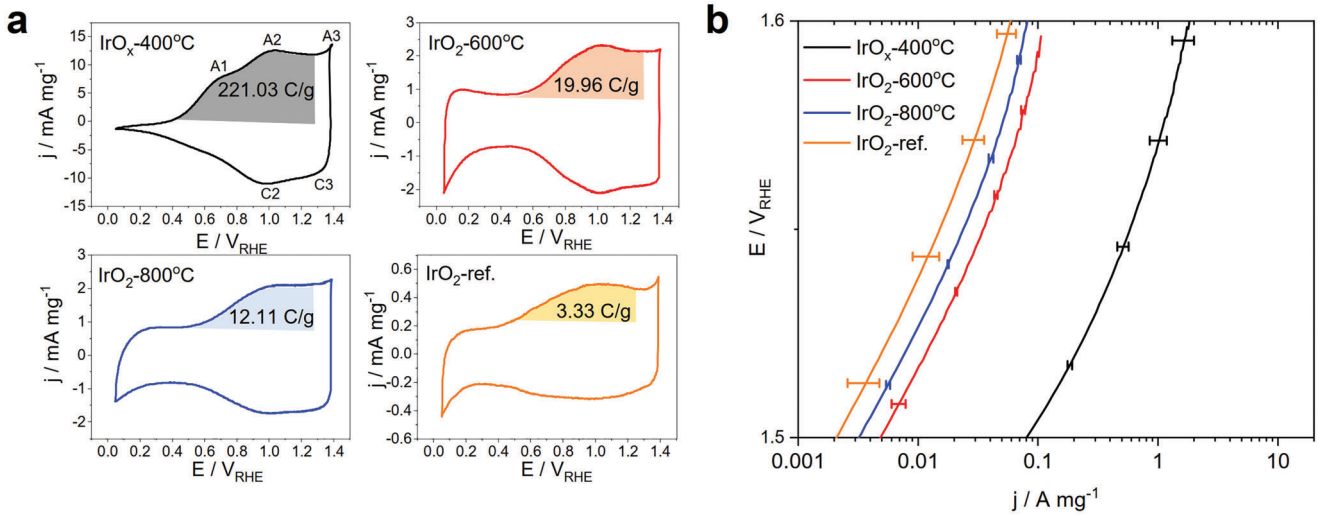

Figure 4. RDE measurements of silica-free iridium oxide catalysts thermally treated at 400, 600, and 800 °C and the reference catalyst in 0.1 M $HClO_4$ a) Mass normalized cyclic voltammetry measured with a scan rate of 50 mV s^{-1} between 0.05–1.4 V_{RHE}. The calculated mass normalized charge within the employed voltage range between 0.4 and 1.3 V_{RHE} is indicated for each material b) Mass normalized activities obtained from first linear sweep voltammetry (LSV) (iR drop corrected) scanning between 1.3 and 1.6 V_{RHE} (highlighted potential region from 1.5 to 1.6 V_{RHE}) with a scan rate of 10 mV s^{-1} and forced convection of 900 rpm. Each sample was measured at least three times and the respective error bars were added.

1.4 V_{RHE} (Figure 4a) indicate the change in the oxidation state of Ir(III) to Ir (IV) and consequently to Ir(V).[33,34] Characteristic of hydrous oxide is the absence of a double-layer- and pseudocapacitive current from iridium oxide due to the loss in conductivity well observed in the potential region below 0.4 V_{RHE}.[34] Previous studies have suggested that the oxygen evolution reaction at amorphous IrO_x may proceed via the lattice oxygen reaction mechanism (LOM), wherein lattice oxygen directly participates in the reaction, leading to high OER activity in such materials.[35,36]

In our study, we conducted Tafel analysis (Figure S6, Supporting Information) to investigate the reaction mechanism in our synthesized samples. However, we could not conclusively identify any discernible differences in the reaction mechanism among the various samples. The Tafel slopes obtained for amorphous IrO_x-400 °C (≈50 mV dec^{-1}), crystalline IrO_2-600 °C (≈60 mV dec^{-1}), and IrO_2-800 °C (≈60 mV dec^{-1}) fell within the typical range of reported values for iridium oxide. Tafel slopes closer to 60 mV dec^{-1} are reported for samples with a higher degree of crystallinity, which is consistent with our findings.[8]

The gradual development of crystal structure with the increase in temperature to 800 °C and consequently the transformation of remaining Ir (III) to Ir (IV) caused a drastic decrease in OER

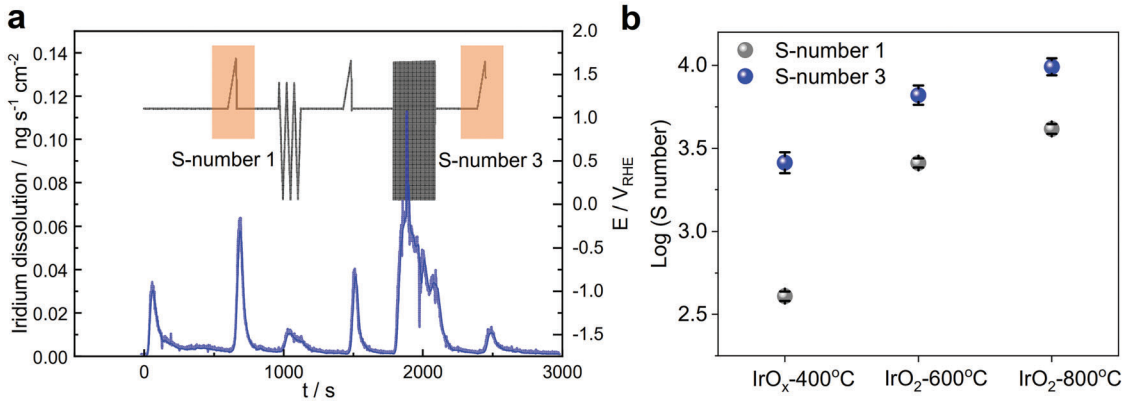

Figure 5. Stability measurement of iridium oxide calcined at 400, 600, and 800 °C measured with a SFC coupled to an ICP-MS in 0.1 M $HClO_4$. a) On-line Ir-dissolution profile (left *y*-axis) exemplarily for IrO_2-800 °C during the stability assessment protocol (right *y*-axis). b) S-number determined by dissolution for all samples during the first (S-number 1, orange box) and third (S-number 3, orange box) linear sweep with a scan rate of 10 mV s^{-1}.

activity of IrO_2-600°C and IrO_2-800 °C. [37] Notably, the observed mass OER activities of IrO_2-600 and IrO_2-800 °C at 1.5 V_{RHE} were 2.45 and 1.65 times higher compared to IrO_2-ref. respectively. The impact of varying surface area between the samples caused by thermal treatment can be excluded by normalizing the OER activity to the active charge capacity extracted from the pseudocapacitive charge between 0.4 and 1.3 V_{RHE} at 50 mV s^{-1}, (c.f. Figure 4a). We note that these normalizations are highly useful to estimate the specific activity but must be considered with care.[13,27,38] The charge decreases almost two orders of magnitude when increasing the synthesis temperature from 400 to 800 °C. Considering the charge normalized OER activity (Figure S10, Supporting Information), the amorphous IrO_x-400 °C remains the most active among the synthesized samples.

To determine the effect of thermal treatment on the electrochemical stability of the synthesized catalysts, we performed online SFC-ICP-MS measurements to quantify iridium dissolution as a function of time and potential range. The measurement protocol (Table S2, Supporting Information) consisted of three linear sweeps from 1.1 V_{RHE} to 5 mA cm^{-2} at 10 mV s^{-1} interposed with 3 CVs in the potential range from 0.05 to 1.4 V_{RHE} and 50 consecutive square wave (SQW) cycles of potential from 0.05 to 1.6 V_{RHE} with a 3 s hold to condition the catalyst. The resulting real-time dissolution profiles of the measured samples are shown in **Figure 5**a, Figures S11–S13 (Supporting Information). To eliminate the impact of the catalyst's surface area, the number of active sites, or the loading, we expressed the intrinsic stability of the catalysts using the stability number (S-number).[13] The calculated S-number values obtained from the total amount of evolved oxygen and dissolved iridium during LSV 1 (S-number 1, orange box, Figure 5a) and LSV 3 (S-number 3, orange box, Figure 5a) demonstrate an inverse trend with activity (Figure 4b), i.e., the stability number increases with an increase in preparation temperature. IrO_2-800 °C exhibits the highest intrinsic stability among the synthesized samples with the initial S-number (S-number 1) being almost one order of magnitude higher than IrO_x-400 °C and comparable to IrO_2-ref. (c.f. Figure S14, Supporting Information).

The reason for the poor stability of IrO_x-400 °C can be ascribed to the loose lattice oxygen bonding network in the amorphous structure compared to the more compact crystalline structure (IrO_2-600 °C and IrO_2-800 °C) that consequently enables direct participation of lattice oxygen in the OER leading to greater iridium dissolution.[13,39] With the increase in temperature and increased crystalline order, the prevalence of hydroxyl surface species can be reduced at the expense of lattice oxygen making IrO_2-600 °C and IrO_2-800 °C less susceptible to dissolution.[39] We find a reciprocal relation between activity and stability strongly indicating the influence of the structure and surface species on the electrochemical properties also on the nanoscale.[4,17]

3. Conclusion

For the first time, the presented synthesis method allows for the synthesis of nanometer sized oxide particles with unprecedented control of particle size and morphology to temperature up to 800 °C. We demonstrate the important role of hydroxyl surface groups for activity on the nanoscale with 40 times higher mass-specific activity compared to the reference iridium oxide catalyst. We highlight how the overall catalyst's structure and the nature of surface oxide species influence the OER activity and stability on the nanoscale. Owing to a protecting silica matrix, the thermal treatment can be performed at various temperatures and annealing times tuning the final properties of the material.[40,41] The increased catalytic stability of IrO_2-800 °C comparable to IrO_2-ref. highlights potential industrial application. These results provide a detailed insight into the performance of size-controlled oxide nanoparticles and illustrate the potential of high surface area oxide nanoparticles for heterogeneous catalysis. The unprecedented control over size at high temperatures can be expanded to other metal-oxide and mixed metal–oxide systems where high crystallinity and small particle dimensions are targeted.

4. Experimental Section

Chemicals: *n*-heptane (99.5% Thermo Scientific Acros), water (D.I.), Brij L4 (Mn ≈ 362, Sigma-Aldrich), Ammonia (28–30%, Supelco), Tetraethyl Orthosilicate (Thermo Scientific Acros), Methanol, Acetone, Hydrofluoric acid (48%, reagent grade, Sigma Aldrich), and Ethanol (99%+, Fisher Chemical).

IrO_2@SiO_2 synthesis procedure: Iridium precursor was dissolved in ultra-pure water to form a solution with a concentration of 62.1 mg mL^{-1}.

Prior to forming a reverse microemulsion, hydrolysis of iridium precursor was done in a 10 mL vial by adding 0.162 mmol iridium precursor aqueous solution to a mixture of 3.8 mL of ultra-pure water and 0.7 mL ammonia (28–30%) aqueous solution. The starting solution was clear and light brownish, the mixture was stirred under ambient conditions until the solution turns purple, which was the indicator that iridium's oxidation state changed from III to IV.

In a round bottom flask, 27 mL of Brij L4 surfactant was dispersed in 120 ml *n*-heptane by stirring for 10 min and additionally by ultrasonication. Subsequently, 4 mL of hydrolyzed iridium oxyhydroxide solution was added dropwise to the mixture forming a reverse microemulsion. Opened to air, the reverse microemulsion was stirred for the next 2 h before 0.75 mL of TEOS was added. Prior to TEOS addition, it was possible to add another 0.7 mL of ammonia to stimulate the formation (pH 10–11) of silica spheres. After 16 h (overnight stirring) for precipitation of particles, 150 ml of methanol was added, stirred vigorously for a couple of minutes, and then let precipitate to settle down for half an hour. At this moment, three separate phases were formed, upper *n*-heptane rich, a middle layer consisting of methanol, and on the bottom, the fluffy light purple precipitate was deposited. The upper layer was decanted and the leftover slurry was centrifuged and washed subsequently with methanol and acetone respectively. The obtained solid phase was dried under vacuum at room temperature for 1 h and prepared for thermal treatment. In total, 200 mg of product was divided into three equal fractions and transferred in alumina crucibles. Thermal treatment was done in a tubular furnace under a synthetic air atmosphere at a flow rate of 10 Nl h^{-1} with a temperature ramp of 2 °C min^{-1} and 3 h of annealing time at temperatures of 400, 600, and 800 °C, respectively.

The removal of silica was done with 1.68% HF-absolute ethanol solution in 50 mL polyethylene bottles mixed by shaker overnight. Note that before starting the experiment with HF, mandatory safety equipment must be worn and a HF first aid kit must be in place.[42] The resulting dispersion was then centrifuged and washed with absolute ethanol and D.I. water. The black wet powder consisting of only IrO_x was then, with the help of absolute ethanol, transferred from the centrifuge tube to a vial and dried under vacuum at 60 °C.

Notably, the synthesis of iridium oxide nanoparticles without silica encapsulation for the in situ STEM comparison study was done in the same manner as described above for IrO_x@SiO_2 excluding the addition of TEOS. Prior to the in situ STEM heating experiment, as-synthesized nanoparticles were washed subsequently with methanol and acetone respectively and dried under vacuum at room temperature for 1 h.

SFC-ICP-MS: *Electrode preparation*: Electrodes with a constant Ir loading of 20 µg cm^{-2} and 20 wt.% Nafion content were prepared by drop-casting 0.2 µL of ink on polished glassy carbon plates (SIGRADUR G, HTW). The drop-casted electrodes were examined with a Keyence VK-X250 confocal laser-scanning microscope to ensure comparable size (roughly 1.3 mm diameter) and quality of the electrode spots.

The silica-free inks were prepared by suspending the investigated catalyst powders in D.I. H_2O (Merck Milli-Q) and adding 2-propanol for stabilization. Nafion perfluorinated resin solution (Alfa Aesar, 5 wt.%) was added afterward to adjust the adhesion of the spots to the glassy carbon substrate. Solvent content of the Nafion solution was accounted for to achieve a mixture of 7/8 H_2O and 1/8 2-propanol. Prior to drop-casting, the inks were sonicated for 15 min, and the pH was adjusted to 11 by adding 1 M KOH to achieve homogeneity.

Dissolution measurements: The SFC-ICP-MS setup with an opening diameter of 2 mm was used as described in prior publications.[13,43] Fresh 0.1 M $HClO_4$ (Merck Suprapur 70% $HClO_4$) was prepared daily by mixing stock solution and DI H_2O. The electrochemical measurements were carried out with Ar-purged 0.1 M $HClO_4$ at a flow rate of 207 µL min^{-1}, connecting the SFC directly to a NexIon 350 spectrometer (Perkin Elmer). A saturated Ag/AgCl reference (Metrohm) and a graphite rod counter electrode were used for measurements. To ensure the constant performance of the ICP-MS, an internal standard solution (10 µg L^{-1} 187Re in 0.1 M $HClO_4$) was added downstream toward the ICP-MS. Calibration curves were recorded daily by measuring freshly prepared solutions of known Ir content (0–5 µg L^{-1} Ir in 0.1 M $HClO_4$).

RDE: The catalyst films for electrochemical activity measurements in the liquid half-cell were prepared by dispersing the investigated catalyst in water (ultrapure grade, VWR) with an ultra-sonic horn (Branson Sonifier), pulse mode at 35% intensity for 30 min onto a glassy carbon electrode (Ø 5 mm) of the RDE tip. The electrodes with a constant IrO_2 loading of 0.5 mg cm^{-2} were prepared by drop-casting of 20 µL of ink on a polished glassy carbon RDE tip. The drop-casted inks were then dried under a constant stream of Argon at room temperature. All the measurements were conducted at room temperature in a multi-neck glass cell in 0.1 M $HClO_4$ (Rotipuran Ultra 70%, Carl Roth GmbH) purged with a constant flow of nitrogen. A saturated Ag/AgCl reference electrode (3 M KCl, Metrohm) and a graphite rod counter electrode were used. The setups were equipped with a Gamry Reference 600 potentiostat and a Radiometer Analytical rotation controller.

XRD Analysis: A Bruker D2 Phaser 2nd Generation was used with a wavelength of Cu K_α = 1.5406 Å. Measurements were taken in a 2-theta range from 20° to 80° with a measurement speed of 0.04°(1.3 s)$^{-1}$ using a background-free silicon sample holder.

HAADF-STEM Measurements: All HAADF-STEM micrographs were obtained using a JEM2100F (JEOL) microscope (200 kV, ZnO/W(100)-emitter). The samples were prepared by dispersion of the investigated material in ethanol with ultra-sonication. Subsequently, 3 × 10 µL of resulting dispersion was dropped onto a Lacey-Carbon coated gold grid (Maxtaform H7).

In Situ STEM and HR-STEM Measurements: The in situ experiments and HR-STEM measurements were conducted on a Hitachi HF5000 environmental STEM at 80 kV and 200 kV acceleration voltages, respectively. For the in situ experiments 10 µL of a catalyst dispersion was dropped onto a MEMS-chip and dried at ambient air for 2 h. With a Hitachi single tilt heating holder, the chip was transferred to the microscope. To remove organic contaminations the chip was heated to 200 °C for 30 min. An internal mass flow controller was then used to set a flow rate of 3 sccm, which resulted in a pressure of ≈5 Pa near the sample. Thereafter, the temperature was increased by 200 °C every 30 min at a rate of 3 °C s^{-1}. For the videos at a magnification of 180 k, the frame time was 60 s and the electron dose per frame was 275.65 e $Å^{-2}$. At 200 k, the electron dose was 340.30 e $Å^{-2}$.

XPS Analysis: All XPS measurements were performed using a SPECS instrument. The samples were excited with monochromatic Al K_α radiation at 1486.74 eV. The emitted photoelectrons were collected using a 150 mm hemispherical energy analyzer (Phoibos 150, SPECS). For each sample a survey scan with a pass energy of 20 eV and high-resolution C 1s, O 1s, Cl 2p, Ir 4p, Ir 4d, and Ir 4f regions with a pass energy of 10 eV were measured. The adventitious C 1s signal of carbon was used for binding energy calibration and assigned to 284.7 eV. The samples were prepared by drop-casting 10 µL of water-based ink of respective sample (concentration 6.5 mg mL^{-1}) on 1 × 1 cm^2 glassy carbon plates. All XPS spectra were deconvoluted using CasaXPS peak fitting software.[44]

TGA Analysis: Standard TGA analysis was performed using STA 449C Jupiter Erich Netzsch GmbH Co. Holding KG, Selb, Germany) by heating 10 mg of sample from 30 to 1100 °C with a temperature ramp of 2 °C min^{-1} and annealing time of 3 h at 1100 °C. The flow rate of synthetic air during the measurement was 100 Nml min^{-1}.

Supporting Information

Supporting Information is available from the Wiley Online Library or from the author.

Acknowledgements

M.M., E.K., J.C., and M.L. acknowledge the Federal Ministry of Education and Research (BMBF) in the framework of NanoMatFutur (SynKat, FK: 03XP0265) for financial support.

Open access funding enabled and organized by Projekt DEAL.

Conflict of Interest

The authors declare no conflict of interest.

Author Contributions

M.M. and M.L. conceived the manuscript. P.P. and M.H. performed in situ heating STEM and HR-STEM experiments. E.S.K. performed HAADF-STEM measurements. M.G., M.M., and S.C. performed SFC ICP-MS measurements and data analysis. J.C. and J.P.H. performed XPS analysis and data analysis. P.P., D.G., and M.M. participated in material synthesis and RDE measurements. All authors discussed the results and assisted during manuscript preparation.

Data Availability Statement

The data that support the findings of this study are available from the corresponding author upon reasonable request.

Keywords

iridium oxide nanoparticles, oxygen evolution reaction, polymer electrolyte membrane water electrolysis

Received: May 12, 2023
Published online: June 13, 2023

[1] U. Babic, M. Suermann, F. N. Büchi, L. Gubler, T. J. Schmidt, *J. Electrochem. Soc.* **2017**, *164*, F387.
[2] M. Ledendecker, J. S. Mondschein, O. Kasian, S. Geiger, D. Göhl, M. Schalenbach, A. Zeradjanin, S. Cherevko, R. E. Schaak, K. Mayrhofer, *Angew. Chem., Int. Ed.* **2017**, *56*, 9767.
[3] Y. Lee, J. Suntivich, K. J. May, E. E. Perry, Y. Shao-Horn, *J. Phys. Chem. Lett.* **2012**, *3*, 399.
[4] N. Danilovic, R. Subbaraman, K.-C. Chang, S. H. Chang, Y. J. Kang, J. Snyder, A. P. Paulikas, D. Strmcnik, Y.-T. Kim, D. Myers, V. R. Stamenkovic, N. M. Markovic, *J. Phys. Chem. Lett.* **2014**, *5*, 2474.
[5] M. Bernt, A. Hartig-Weiß, M. F. Tovini, H. A. El-Sayed, C. Schramm, J. Schröter, C. Gebauer, H. A. Gasteiger, *Chem. Ing. Tech.* **2020**, *92*, 31.
[6] S. T. Hunt, Y. Román-Leshkov, *Acc. Chem. Res.* **2018**, *51*, 1054.
[7] E. Willinger, C. Massué, R. Schlögl, M. G. Willinger, *J. Am. Chem. Soc.* **2017**, *139*, 12093.
[8] D. F. Abbott, D. Lebedev, K. Waltar, M. Povia, M. Nachtegaal, E. Fabbri, C. Copéret, T. J. Schmidt, *Chem. Mater.* **2016**, *28*, 6591.
[9] O. Diaz-Morales, S. Raaijman, R. Kortlever, P. J. Kooyman, T. Wezendonk, J. Gascon, W. T. Fu, M. T. M. Koper, *Nat. Commun.* **2016**, *7*, 12363.
[10] D. Lebedev, M. Povia, K. Waltar, P. M. Abdala, I. E. Castelli, E. Fabbri, M. V. Blanco, A. Fedorov, C. Copéret, N. Marzari, T. J. Schmidt, *Chem. Mater.* **2017**, *29*, 5182.
[11] W. Sun, Y. Song, X.-Q. Gong, L.-m. Cao, J. Yang, *ACS Appl. Mater. Interfaces* **2016**, *8*, 820.
[12] S. Geiger, O. Kasian, B. R. Shrestha, A. M. Mingers, K. J. J. Mayrhofer, S. Cherevko, *J. Electrochem. Soc.* **2016**, *163*, F3132.
[13] S. Geiger, O. Kasian, M. Ledendecker, E. Pizzutilo, A. M. Mingers, W. T. Fu, O. Diaz-Morales, Z. Li, T. Oellers, L. Fruchter, A. Ludwig, K. J. J. Mayrhofer, M. T. M. Koper, S. Cherevko, *Nat. Catal.* **2018**, *1*, 508.
[14] T. Binninger, R. Mohamed, K. Waltar, E. Fabbri, P. Levecque, R. Kötz, T. J. Schmidt, *Sci. Rep.* **2015**, *5*, 12167.
[15] A. Lončar, D. Escalera-López, S. Cherevko, N. Hodnik, *Angew. Chem., Int. Ed.* **2022**, *61*, 202114437.
[16] S. Czioska, A. Boubnov, D. Escalera-López, J. Geppert, A. Zagalskaya, P. Röse, E. Saraçi, V. Alexandrov, U. Krewer, S. Cherevko, J.-D. Grunwaldt, *ACS Catal.* **2021**, *11*, 10043.
[17] S. H. Chang, J. G. Connell, N. Danilovic, R. Subbaraman, K.-C. Chang, V. R. Stamenkovic, N. M. Markovic, *Faraday Discuss.* **2014**, *176*, 125.
[18] D. Escalera-López, S. Czioska, J. Geppert, A. Boubnov, P. Röse, E. Saraçi, U. Krewer, J.-D. Grunwaldt, S. Cherevko, *ACS Catal.* **2021**, *11*, 9300.
[19] Y. Zhao, E. A. Hernandez-Pagan, N. M. Vargas-Barbosa, J. L. Dysart, T. E. Mallouk, *J. Phys. Chem. Lett.* **2011**, *2*, 402.
[20] J. R. Osman, J. A. Crayston, A. Pratt, D. T. Richens, *J. Sol-Gel Sci. Technol.* **2008**, *46*, 126.
[21] S. N. Khadzhiev, K. M. Kadiev, G. P. Yampolskaya, M. K. Kadieva, *Adv. Colloid Interface Sci.* **2013**, *197-198*, 132.
[22] Z. Wu, H. Xiang, T. Kim, M.-S. Chun, K. Lee, *J. Colloid Interface Sci.* **2006**, *304*, 119.
[23] F. Karimi, B. A. Peppley, A. Bazylak, *ECS Trans.* **2015**, *69*, 87.
[24] N. Bestaoui, E. Prouzet, *Chem. Mater.* **1997**, *9*, 1036.
[25] S. J. Freakley, J. Ruiz-Esquius, D. J. Morgan, *Surf. Interface Anal.* **2017**, *49*, 794.
[26] V. Pfeifer, T. E. Jones, J. J. Velasco Vélez, C. Massué, M. T. Greiner, R. Arrigo, D. Teschner, F. Girgsdies, M. Scherzer, J. Allan, M. Hashagen, G. Weinberg, S. Piccinin, M. Hävecker, A. Knop-Gericke, R. Schlögl, *Phys. Chem. Chem. Phys.* **2016**, *18*, 2292.
[27] T. Reier, D. Teschner, T. Lunkenbein, A. Bergmann, S. Selve, R. Kraehnert, R. Schlögl, P. Strasser, *J. Electrochem. Soc.* **2014**, *161*, F876.
[28] R. G. Haverkamp, A. T. Marshall, B. C. C. Cowie, *Surf. Interface Anal.* **2011**, *43*, 847.
[29] A. Hartig-Weiss, M. F. Tovini, H. A. Gasteiger, H. A. El-Sayed, *ACS Appl. Energy Mater.* **2020**, *3*, 10323.
[30] R. V. Mom, L. J. Falling, O. Kasian, G. Algara-Siller, D. Teschner, R. H. Crabtree, A. Knop-Gericke, K. J. J. Mayrhofer, J.-J. Velasco-Vélez, T. E. Jones, *ACS Catal.* **2022**, *12*, 5174.
[31] M. Ledendecker, S. Geiger, K. Hengge, J. Lim, S. Cherevko, A. M. Mingers, D. Göhl, G. V. Fortunato, D. Jalalpoor, F. Schüth, C. Scheu, K. J. J. Mayrhofer, *Nano Res.* **2019**, *12*, 2275.
[32] E. Oakton, D. Lebedev, M. Povia, D. F. Abbott, E. Fabbri, A. Fedorov, M. Nachtegaal, C. Copéret, T. J. Schmidt, *ACS Catal.* **2017**, *7*, 2346.
[33] Z. Pavlovic, C. Ranjan, Q. Gao, M. van Gastel, R. Schlögl, *ACS Catal.* **2016**, *6*, 8098.
[34] V. I. Birss, C. Bock, H. Elzanowska, *Can. J. Chem.* **1997**, *75*, 1687.
[35] O. Kasian, S. Geiger, T. Li, J.-P. Grote, K. Schweinar, S. Zhang, C. Scheu, D. Raabe, S. Cherevko, B. Gault, K. J. J. Mayrhofer, *Energy Environ. Sci.* **2019**, *12*, 3548.
[36] A. Zagalskaya, I. Evazzade, V. Alexandrov, *ACS Energy Lett.* **2021**, *6*, 1124.
[37] C. Daiane Ferreira da Silva, F. Claudel, V. Martin, R. Chattot, S. Abbou, K. Kumar, I. Jiménez-Morales, S. Cavaliere, D. Jones, J. Rozière, L. Solà-Hernandez, C. Beauger, M. Faustini, J. Peron, B. Gilles, T. Encinas, L. Piccolo, F. H. Barros de Lima, L. Dubau, F. Maillard, *ACS Catal.* **2021**, *11*, 4107.
[38] F. Karimi, A. Bazylak, B. A. Peppley, *J. Electrochem. Soc.* **2017**, *164*, F464.
[39] S. Cherevko, T. Reier, A. R. Zeradjanin, Z. Pawolek, P. Strasser, K. J. J. Mayrhofer, *Electrochem. Commun.* **2014**, *48*, 81.
[40] S. T. Hunt, M. Milina, A. C. Alba-Rubio, C. H. Hendon, J. A. Dumesic, Y. Román-Leshkov, *Science* **2016**, *352*, 974.

[41] S. T. Au-Hunt, Y. Au-Román-Leshkov, *J. Vis. Exp.* **2015**, *105*, 53147.
[42] E. Bajraktarova-Valjakova, V. Korunoska-Stevkovska, S. Georgieva, K. Ivanovski, C. Bajraktarova-Misevska, A. Mijoska, A. Grozdanov, *Open Access Maced. J. Med. Sci.* **2018**, *6*, 2257.
[43] S. O. Klemm, A. A. Topalov, C. A. Laska, K. J. J. Mayrhofer, *Electrochem. Commun.* **2011**, *13*, 1533.
[44] N. Fairley, V. Fernandez, M. Richard-Plouet, C. Guillot-Deudon, J. Walton, E. Smith, D. Flahaut, M. Greiner, M. Biesinger, S. Tougaard, D. Morgan, J. Baltrusaitis, *Appl. Surf. Sci. Adv.* **2021**, *5*, 100112.
[45] S. Trasatti, O. A. Petrii, *J. Electroanal. Chem.* **1992**, *327*, 353.